J Appl Electrochem (2008) 38:115–125
DOI 10.1007/s10800-007-9409-y

ORIGINAL PAPER

Electrodeposition of zinc–iron alloy from an alkaline bath in the presence of sorbitol

L. L. Barbosa · Guilherme Antonio Finazzi · P. C. Tulio · I. A. Carlos

Received: 10 October 2006 / Revised: 10 August 2007 / Accepted: 29 August 2007 / Published online: 17 October 2007

Abstract The chronopotentiometric technique was used to analyze the electrodeposition of Fe–Zn film on a Pt electrode. Three different Fe^{3+}/Zn^{2+} molar ratios, Fe26.8 wt.%–Zn73.2 wt.%, Fe46 wt.%–Zn54 wt.% and Fe66.6 wt.%–Zn33.4 wt.%, were used in a solution containing sorbitol as the Fe^{3+}-complexing agent, with a total concentration of the two cations of 0.20 M. Coloration of Fe–Zn films were light gray, dull dark gray and bright graphite, depending on the Fe^{3+}/Zn^{2+} ratios in the deposition bath. The highest stripping to deposition charge density ratio was 47.5%, at 15 mA cm^{-2} in the Fe26.8 wt.%–Zn73.2 wt.% bath. Energy dispersive spectroscopy indicated that the codeposition type of Fe and Zn in the Fe26.8 wt.%–Zn73.2 wt.% and Fe46 wt.%–Zn54 wt.% baths was normal at all j_d tested, while in the Fe66.6 wt.%–Zn33.4 wt.% bath there was a transitional current density from normal to equilibrium codeposition at 50 mA cm^{-2}. Scanning electron microscopy showed that Fe–Zn films of high quality were obtained from the Fe66.6 wt.%–Zn33.4 wt.% and Fe26.8 wt.%–Zn73.2 wt.% baths, since the films were smooth. X-ray analysis of the Zn–Fe films obtained at 15, 25 and 50 mA cm^{-2}, in the Fe26.8 wt.%–Zn73.2 wt.%, Fe46 wt.%–Zn54 wt.% and Fe66.6 wt.%–Zn33.4 wt.% plating baths, suggested the occurrence, in general, of a mixture of $Fe_{11}Zn_{40}$, Fe_4Zn_9, βFe, αFe, Fe_2O_3, Zn and PtZn alloys in the deposit.

Keywords Chronopotentiometry · Electrodeposition · Iron–zinc alloy · Microscopy · Sorbitol · X-ray diffraction

L. L. Barbosa · G. A. Finazzi · P. C. Tulio · I. A. Carlos (✉)
Departamento de Química, Universidade Federal de São Carlos, Via Washington Luiz, CP 676, 13565-905 Sao Carlos, SP, Brazil
e-mail: diac@power.ufscar.br

1 Introduction

Electrodeposited alloys have a large number of industrial and commercial applications [1, 2]. The Fe–Zn alloys in particular exhibit a multiplicity of useful properties, so that interest in studying ways of forming them has been increasing significantly in recent years, in comparison with other alloys of zinc, such as Zn–Ni and Zn–Co [3, 4]. Fe–Zn alloys have also been used to replace cadmium in many applications [4–6]. The properties and characteristics of Fe–Zn alloys depend on both the current density and the ratio of Fe to Zn in the electrodeposited film. Thus, Zn–Fe alloy deposits can vary from very smooth and bright to rough and dull [3, 7, 8]. Regarding the coloration, deposits with a low Fe content (<10%) are light gray, changing progressively to black as Fe rises (>20%) [9–11]. The microhardness of the alloy is higher than that of zinc and increases with increasing Fe content [9]; for example, alloys containing 10% and 40% Fe exhibit microhardness 170 and 300 HV, respectively [7]. Also, an excellent capacity to receive paint and good weldability can be obtained with 50% Fe in the film [4]. However, to be receptive to chromate, the alloy should have 0.5–1.0% Fe [4]. Zn–Fe alloys with 6% Fe exhibit the least corrosion resistance and offer sacrificial protection to steel. Moreover, they deform readily, preserving the adherence of the coating to the substrate [12, 13].

Electroplating baths used for Fe–Zn deposition are either alkaline [1, 14, 15] or acidic [1, 10, 16–20]. Alves et al. [9] observed a high Zn content in the Fe–Zn alloy obtained from an acid deposition bath. The authors observed variation in the film color (from light gray to dark gray) and current efficiency values of 90% over the range of current density studied (0.5–20 A dm^{-2}). Diaz et al. [10] and Abd El Rehim et al. [20] obtained high Zn content

(anomalous deposition) in the alloy film produced from a sulfate-chloride acid bath. Czerwinski et al. [18] observed that adding $SnSO_4$ to an acid sulfate bath (pH = 1.5) containing Fe^{2+} and Zn^{2+} ions changed the morphological characteristics of the films, allowing coatings up to 20 μm thick. Ferreira et al. [19] found that 0.5% Fe in the Fe–Zn alloy, is enough to afford higher resistance to rusting than conventional galvanization. Long et al. [21] evaluated the role of black chromate conversion coatings on the Zn–Fe film produced in an acid sulfate bath. It was concluded that such treatments of the films improve the corrosion behavior of the Zn–Fe alloy. Carlos and Armando [unpublished observation] obtained Fe–Zn films from an alkaline bath with a low Fe content; chromate passivation led to green, yellow, olive and blue films.

Fajardo et al. [8] showed that iron content in the alloy rises with increasing iron content in the sulfate bath and current density. In relation to current efficiency, it was found that increasing the iron percentage in the bath leads to a fall in current efficiency. Barbosa and Carlos [22] studied Fe–Zn chronoamperometric deposition from a sorbitol-alkaline bath containing Fe26.8 wt.%–Zn73.2 wt.% and found that the content of iron in the Fe–Zn films ranged from 74% (–1.36 V) and 70% (–1.4 V) to 40% (–1.6 V). In fact, Fe was the main component of the deposits, its content depending on the deposition potential [22].

In this study we review Fe–Zn deposition from a sorbitol–alkaline plating bath containing various Fe–Zn ratios, using the chronopotentiometric technique. We investigate the influence of current density and bath composition on the current efficiency, coloration, structure and morphology of Fe–Zn films. Scanning electron microscopy (SEM), energy-dispersive spectroscopy (EDS) and X-ray analysis are used to characterize the Fe–Zn deposits.

2 Experimental

All chemicals were analytical grade. Double-distilled water was used throughout. Each electrochemical experiment was performed in a freshly-prepared non-cyanide bath, containing 0.2 M (total) ($FeCl_3$ + $ZnSO_4$) + 3.0 M NaOH + 0.20–0.36 M sorbitol. The distinct bath compositions are given in Table 1. A Pt disk (0.20 cm^2), a Pt plate and an appropriate Luggin capillary containing Hg/HgO/NaOH (1.0 M NaOH, E^0 = 0.0977 V) were employed as working, auxiliary and reference electrodes, respectively. Where indicated, the Pt disk was replaced by Fe (0.50 cm^2) or Zn (0.38 cm^2) disk electrodes. Immediately before the electrochemical measurements, the Pt working electrode was dipped in a concentrated sulphuric-nitric acid solution, while the Fe and Zn disk electrodes were ground with 600 emery paper, after which they were rinsed with water. Chronopotentiometric curves were recorded with a PARC electrochemical system consisting of a model 366A potentiostat/galvanostat. All experiments were carried out at room temperature (25 °C).

Deposits with deposition charge density (q_{dep}) of 5.0 C cm^{-2} under stationary electrode conditions were obtained at various cathodic deposition current densities (j_d). The electrodeposited FeZn films were electrochemically dissolved in a stripping solution of 1.0 M NH_4Cl pH = 1.5 (acidified with HCl) and the stripping to deposition charge density ratios (q_{str}/q_{dep}) were obtained for each electrodeposit [23–27].

X-ray diffraction patterns were produced with filtered Cu-Kα radiation (1.54051 Å), using a D5000 Siemens automatic diffractometer set at 20 kV and 20 mA, running in the $\theta/2\theta$ scanning mode.

Scanning electron microscopy (SEM) photographs were taken with a Stereo Scan 440 Leica electron microscope at 4 nm resolution. Energy dispersive X-Ray spectroscopy (EDS) readings were taken with an eXL Oxford instrument.

3 Results and discussion

3.1 Electrochemical results

Figure 1a shows the chronopotentiometric transients (E/t) of Fe–Zn films electrodeposited on platinum substrate from the bath A at current densities (j_d) from 4 to 50 mA cm^{-2}. Figure 1b shows the E/t transients of alkaline solutions without Fe^{3+} and Zn^{2+} salts, recorded from Fe, Pt, Zn electrodes at 25 mA cm^{-2}. The hydrogen evolution reaction (HER) overpotentials on Fe and Pt are very close (∼ –1.08 and –1.0 V, respectively). On the other hand, the Zn

Table 1 The bath compositions and their designations

Bath composition	Weight percentage (wt.%) of Fe^{3+} and Zn^{2+} in the bath	Bath designation
0.06 M $FeCl_3$ + 0.14 M $ZnSO_4$ + 3.0 M NaOH + 0.2 M sorbitol	Fe^{3+}: 26.8; Zn^{2+}: 73.2	(A)
0.1 M $FeCl_3$ + 0.1 M $ZnSO_4$ + 3.0 M NaOH + 0.28 M sorbitol	Fe^{3+}: 46; Zn^{2+}: 54	(B)
0.14 M $FeCl_3$ + 0.06 M $ZnSO_4$ + 3.0 M NaOH + 0.36 M sorbitol	Fe^{3+}: 66.6; Zn^{2+}: 33.4	(C)

electrode has a greater overpotential (–1.7 V). These results corroborate the overpotentials voltammetrically obtained by Fe and Zn electrodes in this laboratory [21, 25, 26]. Only one plateau can be seen in Fig. 1a at E_p = –1.25 V, for $j_d \leq 15$ mA cm^{-2}, and two plateaus at higher current densities, at ~ –1.55 and –1.60 V. The potentials of these plateaus are between the HER overpotentials on Fe (~ –1.08 V) and Zn (~ –1.7 V). These results imply that the compositions of Fe–Zn films obtained at $j_d \geq 25$ mA cm^{-2} are probably similar, as their deposition potentials are similar (E_d ~ –1.60 V), and different from the films obtained at $j_d < 25$ mA cm^{-2} (E_d ~ –1.25 V), as will be seen later in Sect. 3.4. The Fe–Zn films completely cover the substrate, as observed by light microscopy and SEM (Sect. 3.3).

Figure 2 shows the dissolution voltammograms of Fe–Zn films produced chronopotentiometrically from bath A at various j_d. The stripping solution used was 1.0 M NH_4Cl (pH = 4.5). It is possible to observe, at j_d = 8.0 mA cm^{-2}, a shoulder a_1 (~ –0.60 V) and two dissolution peaks: a_2 (–0.5 V) and a_3 (–0.25 V), and at $j_d \geq 10$ mA cm^{-2}, a dissolution peak b_1 (~ –0.60 V) and a shoulder b_2 (~ –0.30 V).

Figure 3 shows zinc and iron dissolution voltammograms in 1.0 M NH_4Cl (pH = 4.5). The zinc curve shows one peak (~ –0.7 V) and the Fe curve three peaks (~ –0.50, –0.25 and +0.10 V). Comparing Figs. 2 and 3, it can be inferred that the shoulder a_1 (~ –0.60 V, in Fig. 2) and the peak b_1 (~ –0.60 V, in Fig. 2) are probably related to Fe–Zn film dissolution and the dissolution peaks: a_2 (–0.50 V, Fig. 2) and a_3 (–0.25 V, Fig. 2) and shoulder b_2 (~ –0.30 V, Fig. 2) to dissolution and passivation of different Fe species.

Some typical chronopotentiometric transients of deposition of Fe–Zn films from bath B and the corresponding Fe–Zn films dissolution potentiodynamic curves are shown in Figs. 4 and 5, respectively. There is one plateau at large times that varies from –1.2 to –1.4 V in the j_d range from 8 to 25 mA cm^{-2}. On the other hand, for j_d of 50 mA cm^{-2}, the plateau reaches ~ –1.8 V.

Figure 6 shows the E/t transients of Fe–Zn film deposition on platinum in the bath C at j_d from 10 to

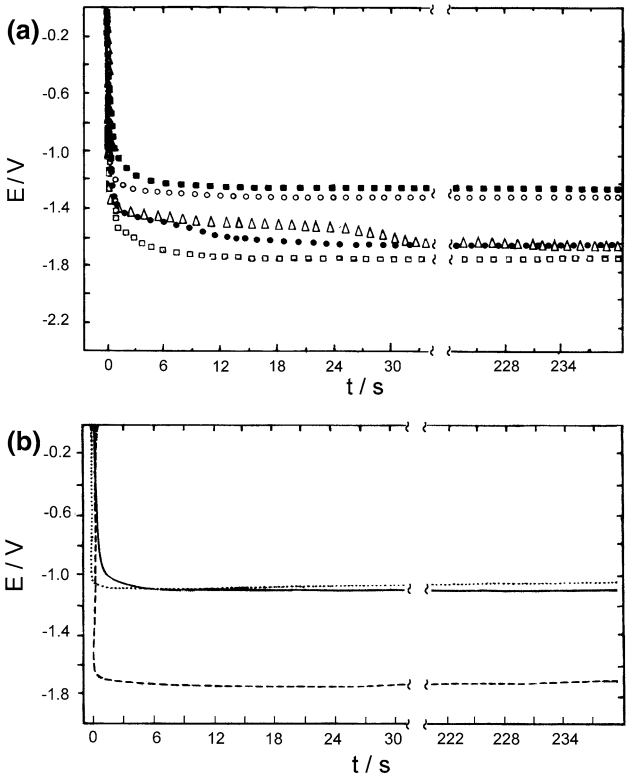

Fig. 1 (**a**) Fe–Zn deposition chronopotentiometric transients obtained at various j_d: 4 mA cm^{-2} (■ ■ ■), 15 mA cm^{-2} (○ ○ ○), 25 mA cm^{-2} (Δ Δ Δ), 35 mA cm^{-2} (• • •) and 50 mA cm^{-2} (□ □ □). q_{dep} = 5 C cm^{-2} on to Pt in bath A (0.06 M $FeCl_3$ + 0.14 M $ZnSO_4$ + 3.0 M NaOH and 0.2 M sorbitol) and (**b**) transients on substrates Fe (——), Pt (·····) and Zn (- - - -) in 3.0 M NaOH + 0.2 M sorbitol, at 25 mA cm^{-2}

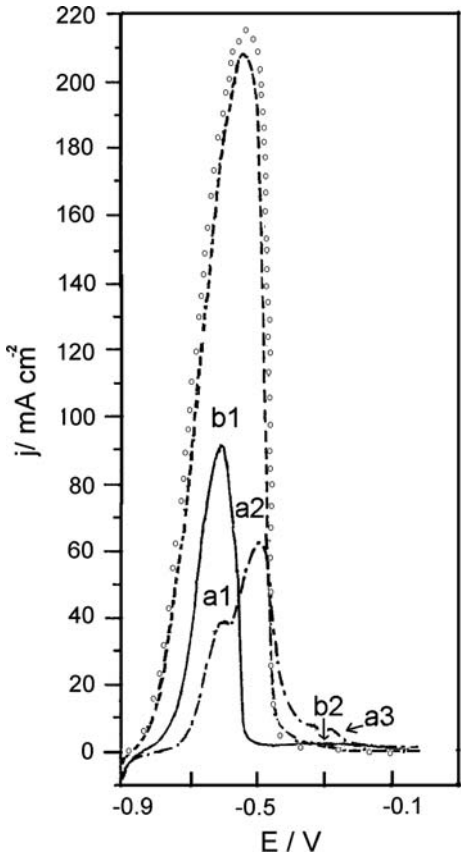

Fig. 2 Stripping curves in 1.0 M NH_4Cl solution (pH 4.5) of the deposits obtained chronoamperometrically from bath A at different j_d: 8 (–°–), 10 (—), 25 (- - - -) and 35 mA cm^{-2} (oooo). v = 30 mV s^{-1}

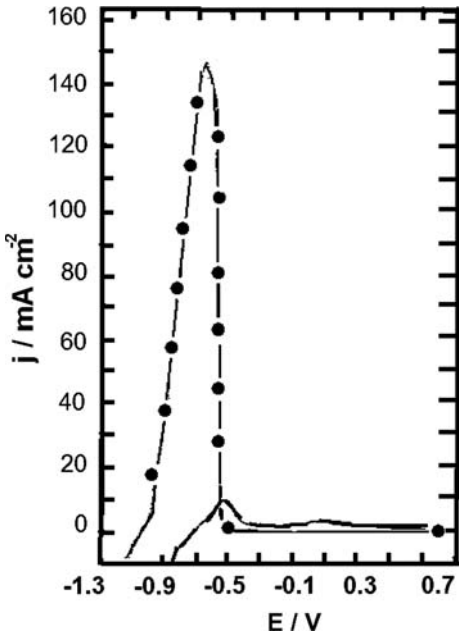

Fig. 3 Dissolution voltammograms of Fe deposit (——) and Zn deposit (–•–•–•–). Dissolution solution 1.0 M NH_4Cl (pH = 4.5); v = 30 mV s^{-1}

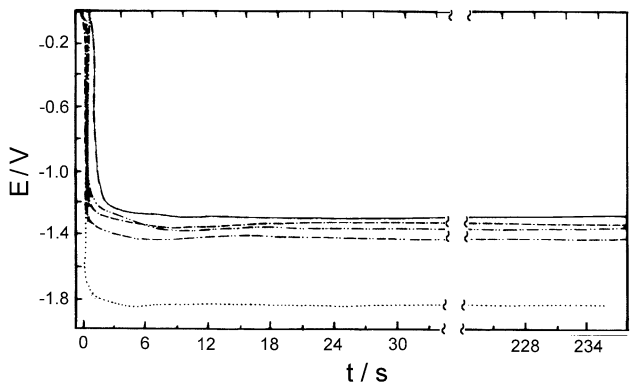

Fig. 4 Fe–Zn deposition chronopotentiometric transients (E/t) on to Pt in bath B (0.10 M $FeCl_3$ + 0.10 M $ZnSO_4$ + 3.0 M NaOH and 0.28 M sorbitol). j_d: 8 mA cm^{-2} (——), 15 mA cm^{-2} (- -.- -.- -), 20 mA cm^{-2} (-..-..-..-), 25 mA cm^{-2} (–..–..–), and 50 mA cm^{-2} (.....)

50 mA cm^{-2}. Raising j_d from 10 to 50 mA cm^{-2} causes the deposition potential to change from ~ –1.2 to –1.8 V. It was observed that the deposition voltammetric curve for bath C was quite different from those for baths A and B since the Fe–Zn deposition kinetics from bath C did not exhibit mass-transport control [25]. By comparing the transients in Fig. 6 with that in Fig. 1 for an intermediate j_d of 35 mA cm^{-2} it can be seen that for bath C this is about 200 mV more positive in potential than that of bath A. On the other hand, for j_d of 50 mA cm^{-2} the quasi-steady state potential attained in bath C (~ –1.8 V) is more negative than that for bath A (~ –1.7 V).

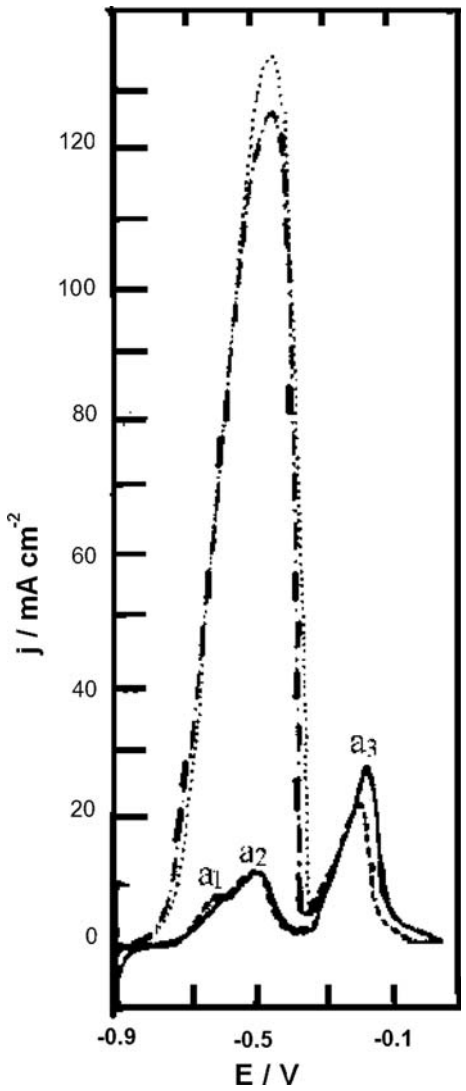

Fig. 5 Dissolution voltammograms of Fe–Zn alloy obtained from bath B at j_d 8 (- - - - -), 10 (——), 25 (–··–) and 35 mA cm^{-2} (·····). Dissolution solution 1.0 M NH_4Cl (pH = 4.5); v = 30 mV s^{-1}

On the basis of Fig. 1b HER occurs simultaneously to Fe–Zn codeposition for all baths and current densities (transients in Figs. 1, 4 and 6).

Stripping curves of the deposits from bath C, obtained chronopotentiometrically at different j_d, in 1.0 M NH_4Cl (pH = 4.5) are shown in Fig. 7. The voltammetric dissolution curve (Fig. 7) for deposits from this bath C was different from those for baths A (Fig. 2) and B (Fig. 5). At a j_d of 10 mA cm^{-2}, four anodic peaks are seen at potentials ~ –0.55, –0.45, –0.25 and +0.5 V. On the other hand, at higher j_d (30 and 35 mA cm^{-2}), only three anodic peaks are formed in the voltammograms, at ~ –0.50, –0.10 and +0.50 V. These peaks, according to the above analysis, probably relate to dissolution and passivation of different species of Fe–Zn alloys and Fe, since the dissolution potentials are in the range between those of Zn and Fe dissolution (Fig. 3).

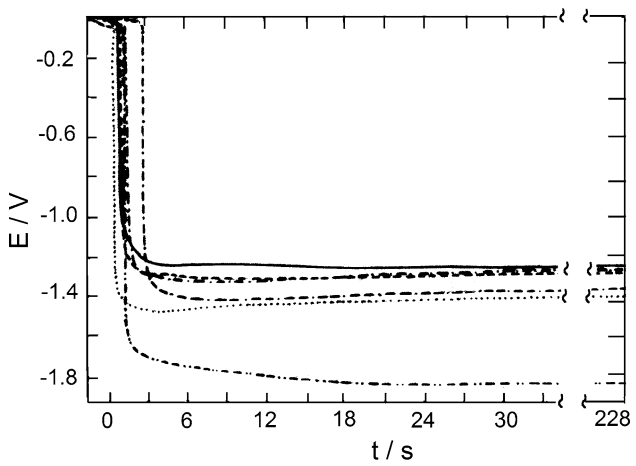

Fig. 6 Fe–Zn deposition chronopotentiometric transients (E/t) on to Pt in bath C (0.14 M + $FeCl_3$ + 0.06 M $ZnSO_4$ + 3.0 M NaOH and 0.36 M sorbitol) at j_d of 10 mA cm^{-2} (——), 15 mA cm^{-2} (- - -), 20 mA cm^{-2} (-·-·-), 30 mA cm^{-2} (- ·-· -), 35 mA cm^{-2} (·····) and 50 mA cm^{-2} (- ·-·- -)

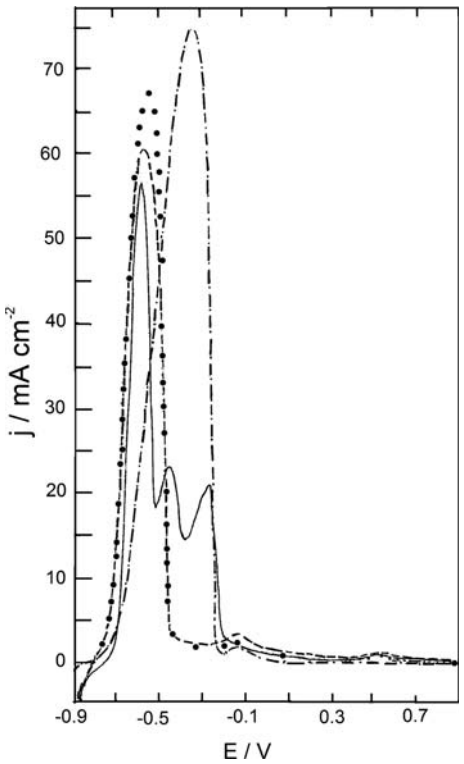

Fig. 7 Dissolution voltammograms of Fe–Zn alloy obtained chronoamperometrically from bath C at j_d of 10 (——), 30 (- - - - -), 35 (• • •) and 50 mA cm^{-2} (-·-·-·-). Dissolution solution: 1.0 M NH_4Cl (pH = 4.5); q_{dep} = 5 C cm^{-2}. v = 30 mV s^{-1}

3.2 Influence of process parameters on the stripping to deposition charge density ratio

Table 2 shows the stripping (q_{str}) to deposition (q_{dep}) charge density ratios (q_{str}/q_{dep}) as a function of bath composition at different current densities. The stripping solution was 1.0 M NH_4Cl pH = 1.5 (acidified with HCl), since the Fe was passivated in 1.0 M NH_4Cl pH = 4.5 [26]. For baths A and B and j_d = 10 mA cm^{-2}, the (q_{str}/q_{dep}) ratio values obtained were very low (8.3% and 2.2%, respectively) and, in general, they improved with increasing j_d in both baths. By contrast, in bath C, the (q_{str}/q_{dep}) ratio value was ~9% at all j_d. Also, the highest (q_{str}/q_{dep}) ratio value of all (47.5%) was observed in the bath with the highest percentage of zinc (bath A). The (q_{str}/q_{dep}) ratios were lower than 100% at all j_d, since the Fe^{3+} and zinc complex are reduced simultaneously with the HER, which is significant, leading to low (q_{str}/q_{dep}) ratio values, especially at j_d = 10 mA cm^{-2}.

These results imply that the films obtained in these baths at $j_d < 15$ mA cm^{-2} were probably a mixture of a large amount of pure Fe with Fe–Zn alloys, while at $j_d > 15$ mA cm^{-2}, the content of pure Fe in the mixture should decrease, due to the formation of other products (Sect. 3.4). This is likely to occur because at $j_d < 15$ mA cm^{-2}, Fe deposits preferentially, as will be seen later in Sect. 3.4. Also, the contribution of HER when $j_d < 15$ mA cm^{-2} was higher than when $j_d > 25$ mA cm^{-2}, so that in the former case the (q_{str}/q_{dep}) ratio was low. It can be seen that the (q_{str}/q_{dep}) ratio is closely associated with both the film composition and j_d.

In relation to film aspect, Table 2 shows that light gray films were obtained from the bath containing a low percentage of iron (bath A) at $j_d > 10$ mA cm^{-2}. In contrast, the films obtained from baths B and C, containing high percentages of iron,, had dark gray and bright graphite coloration, respectively. Also, as will be seen in Sect. 3.4, the Zn–Fe film generally contained Fe_2O_3 formed during the Zn–Fe deposition process, contributing further to the reduction of the (q_{str}/q_{dep}) ratio.

3.3 Surface morphology and EDS analysis of Fe–Zn films

Figure 8a–i shows micrographs of Fe–Zn films obtained from baths A, B and C, respectively, at different j_d. Figure 8a–c and g–i shows that the films from baths A and C, respectively, covered the Pt substrate completely and that morphology did not vary drastically with j_d. Also, these Fe–Zn films were, in general, smooth. On the other hand, Figs. 8d–f shows that the morphology of film deposited from bath B changed drastically with j_d. Barbosa [26] has shown that in bath B, there was change in the mechanism of Fe–Zn electrodeposition, from electron-transfer control (15 mA cm^{-2}) to electron-transfer-diffusion control (25–50 mA cm^{-2}). The results obtained above (Fig. 8) suggested that this change in the deposition process control

Table 2 The (q_{str}/q_{dep}) ratio and coloration of the deposits in iron–zinc electrodeposition baths of various compositions

Deposition bath A (Fe26.8 wt.%–Zn73.2 wt.%)					
j_d/mA cm^{-2}	10	15	20	25	35
$(q_{str}/q_{dep}) \times 100$	8.3	47.5	37.6	32.9	33.4
Film coloration	Dark gray[a]	Light gray	Light gray	Light gray	Light gray
Deposition bath B (Fe46 wt.%–Zn54 wt.%)					
j_d/mA cm^{-2}	10	15	20	25	35
$(q_{str}/q_{dep}) \times 100$	2.2	35.5	30.5	34.0	35.0
Film coloration	Dark gray[a]	Dark gray[b]	Dark gray[b]	Dark gray[a]	Dark gray[a]
Deposition bath C (Fe66.6 wt.%–Zn33.4 wt.%)					
j_d/mA cm^{-2}	10	15	20	25	35
$(q_{str}/q_{dep}) \times 100$	8.9	9.3	9.5	9.4	9.5
Film coloration	Bright graphite	Bright graphite	Bright graphite	Bright graphite	Bright graphite

[a] Bright

[b] Dull

probably had a significant influence on the morphology in the film.

The micrographs also indicate that the films obtained from bath B (Fig. 8d–f) are probably rougher than those obtained from other baths A (Fig. 8a–c) and C (Fig. 8g–i). In fact, these morphological data are corroborated by the dullness of the Fe–Zn films produced in bath B (Table 2).

The EDS elemental analysis results of Fe–Zn films produced at several j_d from baths A, B and C are plotted in Fig. 9 to show the relations between the alloy and bath compositions for each current density and between cathodic current density and alloy composition for each deposition bath solution (Fig. 10).

Figure 9 shows the variation of the iron content in the Fe–Zn films with the weight percentage of iron in the bath. The diagonal composition reference line (CRL) represents Fe–Zn films with the same composition as the bath, then, Fe and Zn codeposition type is equilibrium [1]. Most of the data in Fig. 9 lie well above the CRL, except those for j_d of 50 mA cm^{-2} and deposition bath C and for j_d of 25 and 50 mA cm^{-2} and bath B. The data points above the CRL indicate that the alloys are richer in iron than the baths from which they were obtained (normal codeposition type [1]). The position of the data points in Fig. 9 with respect to the CRL shows that iron was by far the more readily deposited metal.

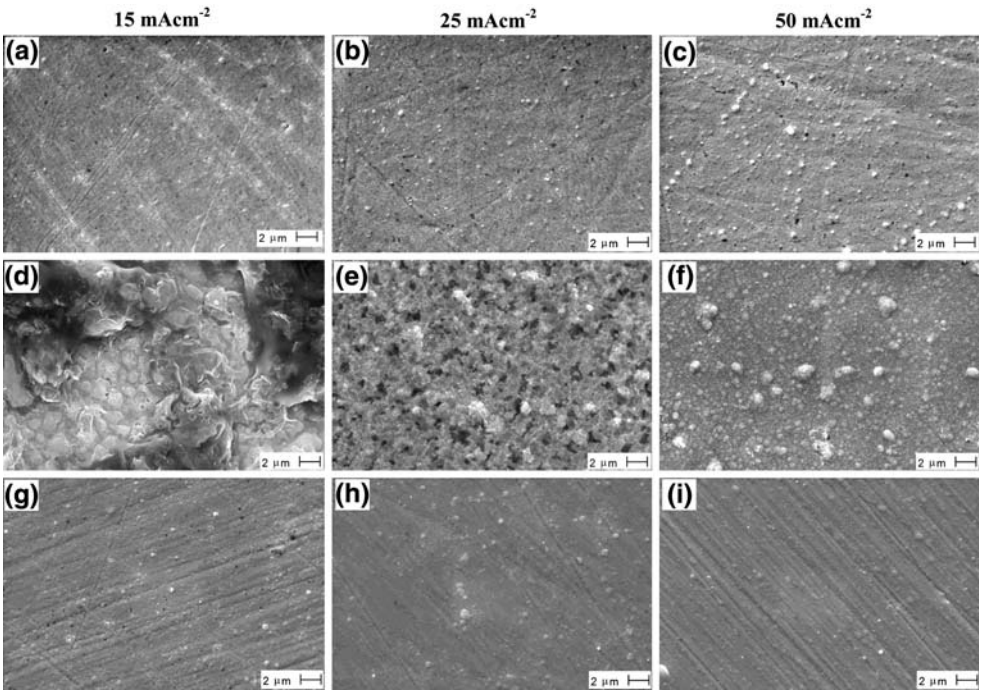

Fig. 8 Scanning electron micrographs of Fe–Zn deposits obtained at constant deposition current densities of 15, 25 and 50 mA cm^{-2}: (**a**), (**b**) and (**c**) for bath A; (**d**), (**e**) and (**f**) for bath B and (**g**), (**h**) and (**i**) for bath C. q_{dep} = 5.0 C cm^{-2}

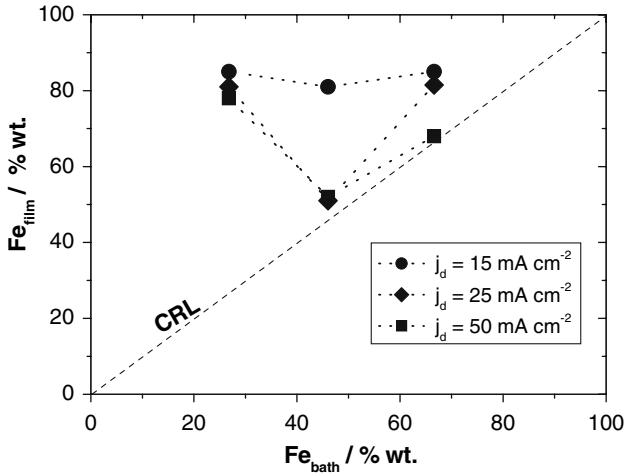

Fig. 9 Relation between the percentage of iron in the deposit and in the deposition bath obtained at different j_d indicated in the figure. The line (- - - - -) is the composition reference line (CRL). The connecting lines are only guidelines

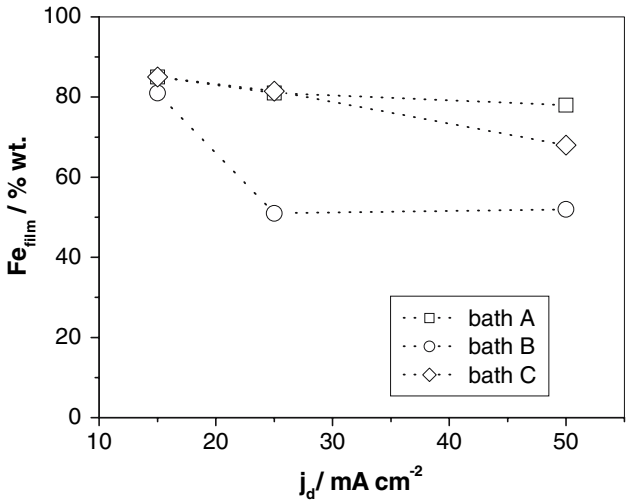

Fig. 10 Effect of current density on the iron content of Fe–Zn alloys electrodeposited from various different baths, indicated in the figure. The connecting lines are only guidelines

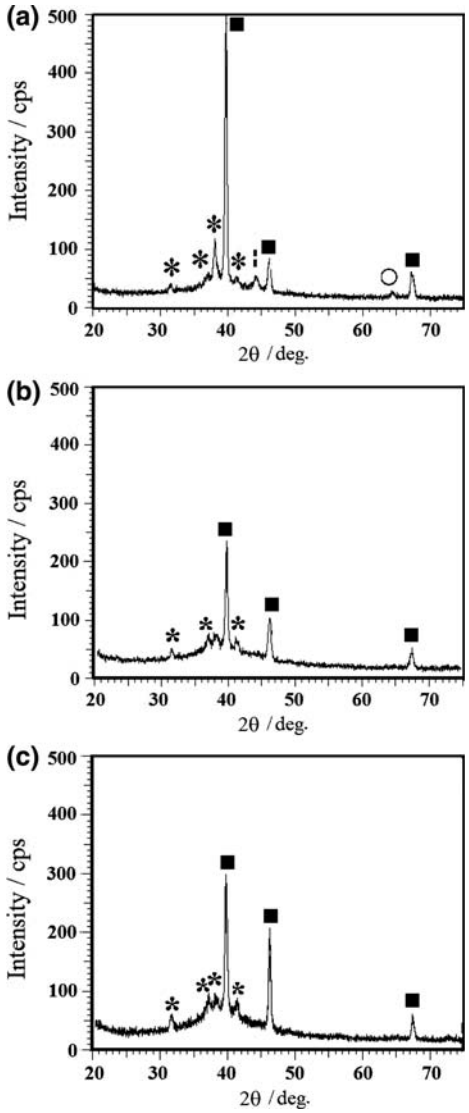

Fig. 11 X-ray diffractograms of Fe–Zn alloy obtained at constant current density: (**a**) 15 mA cm^{-2}, (**b**) 25 mA cm^{-2} and (**c**) 50 mA cm^{-2}. Deposition solution bath A (0.06 M $FeCl_3$ + 0.14 M $ZnSO_4$ + 3.0 M NaOH and 0.2 M sorbitol). q_{dep} = 5.0 C cm^{-2}. *, $Fe_{11}Zn_{40}$; ■, Pt; ○, βFe, ▌, αFe

The results obtained above (Fig. 9) suggest that the changes in the deposition process control, as reported above [26], probably had a significant influence, not only on the film morphologies (Fig. 8d–f), but also on the iron content in the film.

Figure 10 illustrates the influence of j_d on the alloy composition for the different deposition solutions. It can be inferred that the Fe and Zn codeposition type was normal from baths A and B. The film composition obtained from bath C has the same even characteristics as in bath A for 15 an 25 mA cm^{-2} and thus the codeposition type remains normal. However, for j_d = 50 mA cm^{-2}, the iron percentage in the film was 68 wt.%, which is very close to those of the CRL (Fig. 9). Thus, in this case, the codeposition type was near equilibrium, since the deposit and bath had, approximately, the same percentages of Fe and Zn.

It may be concluded that the alloy composition changes with both bath composition and j_d, and that the type of codeposition changed, from normal to near equilibrium, in bath C. Thus, it can be inferred that there is a transitional current density, from normal to near-equilibrium codeposition, in the range from 25 to 50 mA cm^{-2} for Fe–Zn films obtained chronopotentiometrically from bath C. Our group showed recently [22] that for deposition in bath A, depending on the deposition potential, the content of iron in Fe–Zn films ranged from 73 wt.% (–1.36 V) and

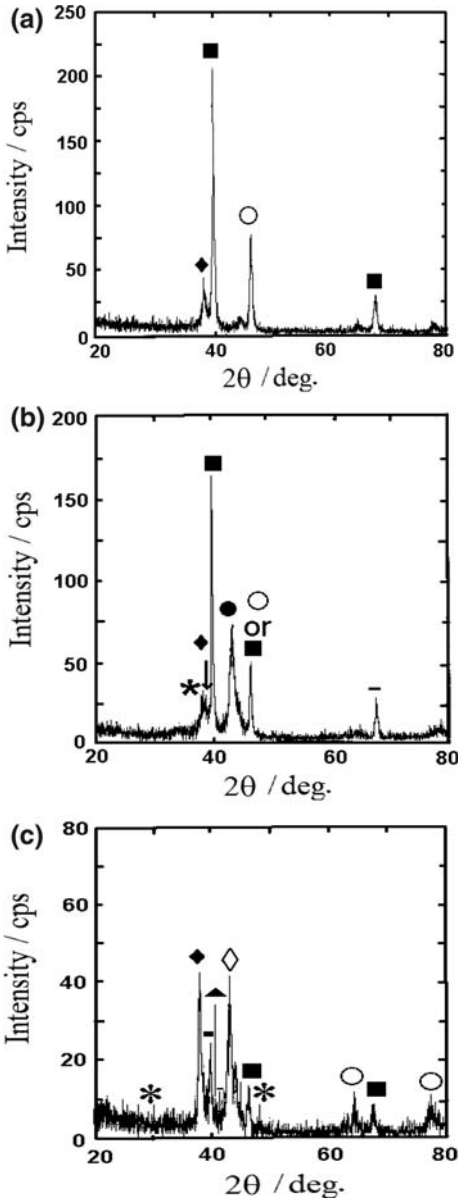

Fig. 12 X-ray diffractograms of Fe–Zn alloy obtained at constant current density: (**a**) 15 mA cm^{-2}, (**b**) 25 mA cm^{-2} and (**c**) 50 mA cm^{-2}. Deposition solution bath B (0.10 M $FeCl_3$ + 0.10 M $ZnSO_4$ + 3.0 M NaOH and 0.28 M sorbitol). q_{dep} = 5.0 C cm^{-2}. *, $Fe_{11}Zn_{40}$; ■, Pt; ○, βFe; ♦, Fe_2O_3; ◇, Zn; •, Fe_4Zn_9; ▲, $FeZn_{15}$; –, $FeZn_{11}$

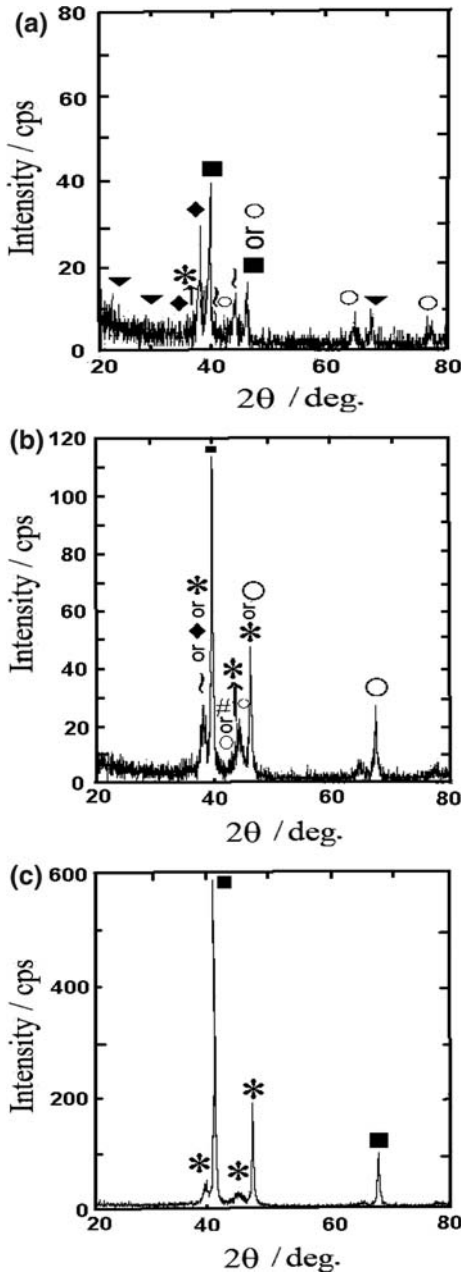

Fig. 13 X-ray diffractograms of Fe–Zn alloy obtained at constant current density: (**a**) 15 mA cm^{-2}, (**b**) 25 mA cm^{-2} and (**c**) 50 mA cm^{-2}. Deposition solution bath C (0.14 M $FeCl_3$ + 0.06 M $ZnSO_4$ + 3.0 M NaOH and 0.36 M sorbitol). q_{dep} = 5.0 C cm^{-2}. *, $Fe_{11}Zn_{40}$; ■, Pt; ○, βFe; ♦, Fe_2O_3; ⟆, Pt_5Zn_{21}; ▼, Pt_3Zn; -, Pt_7Zn_{12}; #, $FeZn_7$

70 wt.% (–1.4 V) to 40 wt.% (–1.6 V). Thus, Fe is the main component of the deposits formed at –1.36 and –1.40 V, whereas Zn is predominant at –1.60 V. On the other hand, the results above show that in chronopotentiometric conditions, in bath A, the iron content was always higher than zinc, independently of j_d. These are significant results as they show that, for this Fe–Zn ratio in the plating bath, the deposition technique governs the iron content in the deposit.

3.4 X-ray analysis of the Fe–Zn deposits

Figures 11–13 show typical X-ray diffraction patterns of deposits obtained from baths A, B and C at various j_d for q_d = 5.0 C cm^{-2}. The observed crystallographic distances (d(*hkl*)), obtained from these patterns are compared with expected values (d_{exp}), described in JCPDS [28], in Tables 3–5. Some diffraction lines are easily assigned to

Table 3 Observed interplanar distances, d*(hkl)$_{obs}$*, of X-ray diffraction pattern of Fe–Zn deposits obtained from bath A at various j_d. q_{dep} of 5.0 C cm^{-2}

$d_1(hkl)_{obs}$ (j_d = 15 mA cm^{-2})	$d_2(hkl)_{obs}$ (j_d = 25 mA cm^{-2})	$d_3(hkl)_{obs}$ (j_d = 50 mA cm^{-2})	d_{exp} (Pt)	d_{exp} (αFe)	d_{exp} (βFe)	d_{exp} ($Fe_{11}Zn_{40}$)
2.83	2.83	2.83				2.8450
2.39	2.39	2.39				2.4040
2.36		2.36				2.3430
2.25	2.25	2.25	2.2650			
2.19	2.19	2.19				2.1970
2.12						2.1200
2.03				2.0268		
1.96	1.96	1.96	1.9616			1.8870
1.44				1.4332	1.4400	
1.38	1.38	1.38	1.3873			

The expected values (d_{exp}) are from JCPDS [28]: Pt, αFe, βFe and $Fe_{11}Zn_{40}$ above 10% of relative intensity. Observed values for platinum were obtained experimentally

Table 4 The same as Table 3 for Fe–Zn deposits obtained from the bath B. q_{dep} of 5.0 C cm^{-2}

$d_1(hkl)_{obs}$ (j_d = 15 mA cm^{-2})	$d_2(hkl)_{obs}$ (j_d = 25 mA cm^{-2})	$d_3(hkl)_{obs}$ (j_d = 50 mA cm^{-2})	d_{exp} (Pt)	d_{exp} (Zn)	d_{exp} (βFe)	d_{exp} (Fe_4Zn_9)	d_{exp} ($Fe_{11}Zn_{40}$)	d_{exp} (Fe_2O_3)	d_{exp} ($FeZn_{15}$)
		2.95					2.998		
2.35	2.36	2.36					2.3430	2.360	
2.26	2.26	2.26	2.2650						
		2.16							2.1600
	2.10	2.10		2.0910		2.1160			
1.96	1.97	1.95	1.9616		1.9700				
		1.89					1.8870		
		1.44			1.4400				
1.38	1.38	1.38	1.3873						
		1.23			1.2340				

The expected values (d_{exp}) are from JCPDS [28]: Pt, βFe, Fe_2O_3, Fe_4Zn_9, $Fe_{11}Zn_{40}$ and Zn above 10% of relative intensity. Observed values for platinum were obtained experimentally

d_{exp} (Pt). The peaks at d_{obs} of 2.26 and 1.38 are attributed to Pt, since the d_{exp} (Pt) value is 2.2650 (I/I_o = 100%) and 1.3873 (I/I_o = 31%). Also the peak at d_{obs} of 1.96 is attributed to Pt and not $Fe_{11}Zn_{40}$, since d_{exp} (Pt) is 1.9616 (I/I_o = 53%) and d_{exp} ($Fe_{11}Zn_{40}$) 1.9620 (I/I_o = 20%).

Table 6 shows the phases in the Fe–Zn deposits identified in this X-ray analysis. The X-ray analysis of Fe–Zn films shows the production of various Fe–Zn alloys and also of Pt–Zn alloys (Tables 3–6), corroborating the results of Chu [29], which showed the production of Pt–Zn alloys during zinc deposition on a platinum substrate.

4 Conclusions

For the electrodeposition of Fe–Zn films from alkaline solutions employing the chronopotentiometric technique the conclusions as follows:

The plateaux in the chronopotentiometric transients for Fe–Zn electrodeposition are associated with Fe–Zn alloy deposition and the hydrogen evolution reaction occurring simultaneously.

EDS results confirmed that the alloy composition change with bath composition and j_d and that the type of codeposition changes from normal to near equilibrium in bath C as j_d increases. This implies that there is a transitional current density in the range 25 to 50 mA cm^{-2} for Fe–Zn films obtained chronopotentiometrically from bath C.

The (q_{str}/q_{dep}) ratio values at j_d of 15 mA cm^{-2} decreased from ~48% from bath less rich in Fe^{3+} (bath A) to 9% from the richer one (bath C). The coloration of films obtained from bath A varied between bright dark gray and light gray, and for baths B and C between dull dark gray and bright graphite, respectively.

SEM results showed that the morphological characteristics of the films were closely related, in general, to both deposition current density and bath composition and that the deposits obtained from baths A and C were smooth, while those from the bath B were rough.

Table 5 The same as Tables 3 and 4 for Fe–Zn deposits obtained from the bath C. q_{dep} of 5.0 C cm^{-2}

d_1 $(hkl)_{obs}$ (j_d = 15 mA cm^{-2})	d_2 $(hkl)_{obs}$ (j_d = 25 mA cm^{-2})	d_3 $(hkl)_{obs}$ (j_d = 50 mA cm^{-2})	d_{exp} (Pt)	d_{exp} (Zn)	d_{exp} (Pt_5Zn_{21})	d_{exp} (βFe)	d_{exp} (Fe_4Zn_9)	d_{exp} ($Fe_{11}Zn_{40}$)	d_{exp} (Pt_3Zn)	d_{exp} (Fe_2O_3)	d_{exp} (FeO)	d_{exp} (Pt_7Zn_{12})	d_{exp} (αFe)
4.44					4.44								
3.71										3.6840			
2.79							2.8410		2.770				
2.47				2.4730			2.5920				2.4700		
2.36	2.33	2.34			2.3500			2.3430		2.36			
2.26	2.26	2.28	2.2650										
2.15	2.15				2.130							2.161	
2.11						2.1200							
2.07	2.05	2.04		2.0910				2.0640				2.053	2.0268
		1.96	1.9616	1.6870				1.962					
1.44						1.4400							
1.38	1.38	1.38	1.3873					1.3770	1.378			1.381	
1.23						1.234							

The expected values (d_{exp}) are from JCPDS [28]: Pt, βFe, Fe_2O_3, Fe_4Zn_9, $Fe_{11}Zn_{40}$ and Zn above 10% of relative intensity. Observed values for platinum were obtained experimentally

Table 6 The phases in the Fe–Zn deposits, obtained from baths A, B and C at different current densities, identified in the X-ray analysis of the films

Bath	j_d = 15 mA cm^{-2}	j_d = 25 mA cm^{-2}	j_d = 50 mA cm^{-2}
A	$Fe_{11}Zn_{40}$; Pt; αFe; βFe	$Fe_{11}Zn_{40}$; Pt	$Fe_{11}Zn_{40}$; Pt
B	Fe_2O_3; Pt; βFe	$Fe_{11}Zn_{40}$; Fe_2O_3; Zn; Pt; Fe_4Zn_9; βFe	$Fe_{11}Zn_{40}$; Zn; Fe_2O_3; Pt; βFe; $FeZn_{15}$; $FeZn_{11}$
C	$Fe_{11}Zn_{40}$; $FeZn_7$; Fe_2O_3; Pt; βFe; Pt_5Zn_{21}; Pt_3Zn; Pt_7Zn_{12}	$Fe_{11}Zn_{40}$; $FeZn_7$; Fe_2O_3; Pt; βFe; Pt_5Zn_{21}; Pt_3Zn; Pt_7Zn_{12}	$Fe_{11}Zn_{40}$; Pt; Pt_7Zn_{12}

X-ray analysis of the Zn–Fe films, obtained from baths A, B and C at different j_d, suggested the occurrence, in general, of a mixture of Zn–Fe alloys, Zn, αFe, βFe, Fe_2O_3 and Pt–Zn alloys in the deposits.

References

1. Brenner A (1963) Electrodeposition of alloys, vol 1. Academic Press, New York
2. Lowenheim LA (1974) Modern electroplating. John Wiley & Sons, New York
3. Jimenéz A (2003) Tratam Superf 120:26
4. Pushpavanam M (2000) Bull Electrochem 16:559
5. Zaki N (1999) Prod Finish 63:53
6. Short NR, Dennis JK (1997) Trans Inst Met Finish 75:47
7. Wit K, Boeck A, Cooman BC (1999) J Mat Eng Perform 8:531
8. Rodriguez Fajardo AA, Degrez M, Winand R (1989) Oberf Surf 8:20
9. Alves VF, Ferreira JZ (2001) Contribuição ao estudo da liga Zn–Fe obtida por eletrodeposição. In: Proceedings of the XII Simpósio Brasileiro de Eletroquímica e Eletroanalítica (XII SIBEE), Gramado, Brasil
10. Diáz SL, Mattos OR, Barcia OE, Miranda FJF, Wiart R (2001) Eletrodeposição de Fe e ligas ZnFe em eletrólito de sulfato: efeito do pH. In: Proceedings of XII Simpósio Brasileiro de Eletroquímica e Eletroanalítica (XII SIBEE), Gramado, Brasil
11. Jayakumar ND (1998) Ind Metal Finish 4:711
12. Ravindran V, Jayakrishnan S, Sridevi R, Rajakumari R, Muralidharan VS (2004) Bull Electrochem 20:118
13. Hixon HG, Sherwood PMA (2001) J Phys Chem 105B:3957
14. Budman E, Sizelove RR (1999) Metal Finish 97:334
15. Gardner RE (1994) Control and preparation of an alkaline zinc–iron solution. In: Proceedings of the VII Encontro Brasileiro em Tratamento de superfícies (VII EBRATS), São Paulo, Brazil, pp 1–13
16. Gómez E, Pelaez E, Vallés E (1999) J Electroanal Chem 469:139
17. Gomez E, Alcobe X, Vallés E (1999) J Electroanal Chem 475:66
18. Czerwinski F, Szpunar JA, Kondo K (1998) J Mat Sci 33:2589
19. Ferreira JZ, Fermiano VM, Fuhr J (1995) Eletrodeposição de ligas Zinco-Ferro. Proceedings of the 18ª Reunião Anual da Sociedade Brasileira de Química (18ª RASBQ), Caxambu, Brasil, pp EQ 078
20. Abd El Rehim SS, Emad M, Khaled M, Fettouhi M (2001) Trans Inst Metal Finish 79:95
21. Long ZL, Zhou YC, Xiao L (2003) Appl Surf Sci 218:123

22. Barbosa LL, Carlos IA (2006) Surf Coat Technol 201:1695
23. Abd El Rehim SS, Abd El Wahaab SM, Fouad EE, Hasan HH (1994) J Appl Electrochem 24:350
24. Vanden Branden P, Dumont A, Winand R (1994) J Appl Electrochem 24:2001
25. Carlos IA, Souza CAC, Pallone EMJA, Francisco RHP, Cardoso V, Lima-Neto BS (2000) J Appl Electrochem 30:987
26. Barbosa LL (2005) Desenvolvimento e caracterização eletroanalítica e espectrofotométrica de banhos alcalinos, na presença de sorbitol e/ou glicerol e EDTA, para eletrodeposição de ligas de Fe/Zn e caracterização química, física e morfológica dos filmes de Fe/Zn. PhD. Thesis, Universidade Federal de São Carlos, São Carlos, Brazil
27. Barbosa LL, Brito GAO, Lopes MC, Broggi RL, Carlos IA (2005) Electrochim Acta 50:4710
28. Joint Committee on Powder Diffraction Standards, JCPDS (2000) International Centre for Diffraction Data. Powder Diffraction File—PDF-2. Database Sets 1–49. Pennsylvania, ICDD (CD-ROM)
29. Chu MG, MCBreen J, Adzic G (1981) J Electrochem Soc 128:2281